JOURNAL OF GEOPHYSICAL RESEARCH, VOL. 99, NO. B11, PAGES 21,983–22,000, NOVEMBER 10, 1994

Modeling of periodic great earthquakes on the San Andreas fault: Effects of nonlinear crustal rheology

Ze'ev Reches
Department of Geology, Hebrew University of Jerusalem, Jerusalem, Israel

Gerald Schubert
Department of Earth and Space Sciences and Institute of Geophysics and Planetary Physics, University of California, Los Angeles

Charles Anderson
Engineering Sciences & Applications, Los Alamos National Laboratory, Los Alamos, New Mexico

Abstract. We analyze the cycle of great earthquakes along the San Andreas fault with a finite element numerical model of deformation in a crust with a nonlinear viscoelastic rheology. The viscous component of deformation has an effective viscosity that depends exponentially on the inverse absolute temperature and nonlinearly on the shear stress; the elastic deformation is linear. Crustal thickness and temperature are constrained by seismic and heat flow data for California. The models are for anti plane strain in a 25-km-thick crustal layer having a very long, vertical strike-slip fault; the crustal block extends 250 km to either side of the fault. During the earthquake cycle that lasts 160 years, a constant plate velocity $v_p/2 = 17.5$ mm yr^{-1} is applied to the base of the crust and to the vertical end of the crustal block 250 km away from the fault. The upper half of the fault is locked during the interseismic period, while its lower half slips at the constant plate velocity. The locked part of the fault is moved abruptly 2.8 m every 160 years to simulate great earthquakes. The results are sensitive to crustal rheology. Models with quartzite-like rheology display profound transient stages in the velocity, displacement, and stress fields. The predicted transient zone extends about 3–4 times the crustal thickness on each side of the fault, significantly wider than the zone of deformation in elastic models. Models with diabase-like rheology behave similarly to elastic models and exhibit no transient stages. The model predictions are compared with geodetic observations of fault-parallel velocities in northern and central California and local rates of shear strain along the San Andreas fault. The observations are best fit by models which are 10–100 times less viscous than a quartzite-like rheology. Since the lower crust in California is composed of intermediate to mafic rocks, the present result suggests that the in situ viscosity of the crustal rock is orders of magnitude less the rock viscosity determined in the laboratory.

Introduction

The elastic rebound model of *Reid* [1910] implies that elastic strain is accumulated during a long interseismic period that is followed by local yielding and fast fault slip during an earthquake. This process repeats itself in irregular periods known as earthquake cycles. *Reid's* [1910] model for a perfect elastic medium cannot explain the time-dependent behavior exhibited by actual earthquakes. For example, almost all large earthquakes are followed by aftershock activity that lasts for months to years; the energy release of the aftershocks decays exponentially with time. While the locations and mechanisms of aftershocks have been analyzed in terms of elastic models [e.g., *Oppenheimer et al.*, 1988], the duration of aftershock activity and the mode of its decay require a viscoelastic rheology. Additionally, postseismic deformation, revealed by geodetic measurements [*Thatcher*, 1975], and the occurrence of creep events that last hours to weeks along parts of the San Andreas fault suggest that the crust cannot be regarded as a simple elastic solid. Finally, it is widely accepted that continental crustal rocks below 10–15 km deform according to a nonlinear viscoelastic rheology (Figure 1) [e.g., *Kirby*, 1983]. Nevertheless, geodetic observations of crustal de-

Paper number 94JB00334.
0148-0227/94/94JB-00334$05.00

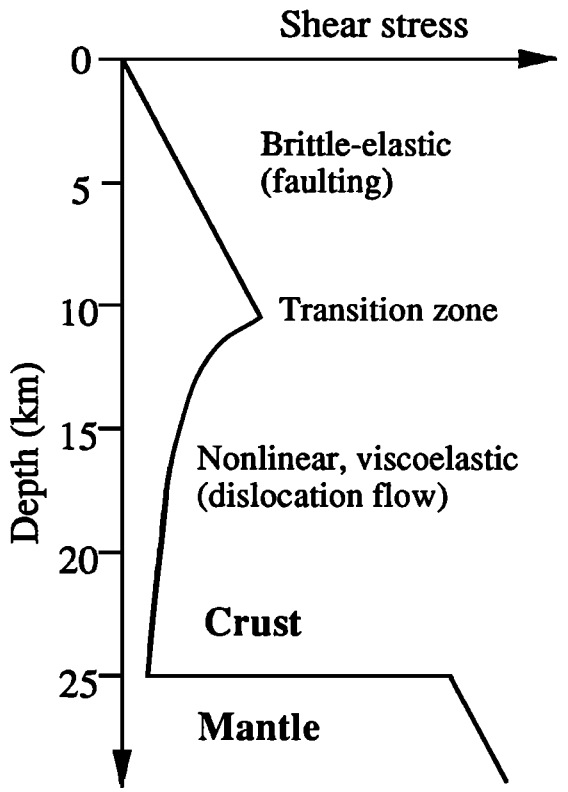

Figure 1. General rheology of the continental crust [after *Brace and Kohlstedt,* 1980].

formation between earthquakes are frequently modeled by dislocations in an elastic half-space. These dislocations must be placed at great depths (below 10 km) to obtain good fits to geodetic data [e.g., *Prescott and Yu,* 1986].

Several viscoelastic models have been proposed to explain these and other shortcomings of the elastic models [*Nur and Mavko,* 1974; *Savage and Prescott,* 1978; *Thatcher,* 1983; *Turcotte et al.,* 1984; *Li and Rice,* 1987; *Lyzenga et al.,* 1991]. *Nur and Mavko* [1974] considered a long strike-slip fault within an elastic layer that overlies a viscoelastic half-space. In their model, the depth of the fault D is equal to or smaller than the thickness of the elastic layer H. The earthquake cycles were modeled by uniform slip along the fault and sequential loading of the elastic layer and the underlying viscoelastic medium, followed by time-dependent relaxation of the linear (Maxwell) viscoelastic substrate. The substrate transfers shear stresses back to the elastic layer, generating transient stress and velocity fields. *Thatcher* [1983] compared predictions of the *Nur and Mavko* [1974] and elastic half-space models with geodetic observations along the San Andreas fault but was only able to provide weak constraints on the crustal structure and the intensity of elastic-viscoelastic coupling. The difficulty in obtaining stronger constraints probably stems from two sources. The available geodetic observations are limited, in time and location, and they include large intrinsic noise [e.g., *Thatcher,* 1983, Figures 12 and 13]. Also, the analyzed configurations and rheologies are perhaps too simplified to account for real crustal mechanics.

Li and Rice [1987] also analyzed the earthquake cycle within an elastic-viscoelastic crust. Their model includes an upper elastic layer of thickness H, with a long strike-slip fault that penetrates to depth D, where $D < H$. The elastic layer is underlain by a viscoelastic (Maxwell) layer of thickness h. Analytic solutions to the deformation during the earthquake cycle were obtained by using a modified Elsasser approximation. This model is compared below with the numerical results of the present modeling.

We investigate here the cycle of great earthquakes along the San Andreas fault with a finite element code (ABAQUS). The rock rheology is assumed to be temperature dependent and nonlinear; crustal thickness and temperature are constrained by seismic and heat flow data. *Lyzenga et al.* [1991] have also used a finite element approach to study deformation during a series of earthquakes along a model San Andreas fault in a medium with nonlinear, depth-dependent rheology. The focus of their study was the influence of fault strength on the great earthquake recurrence time. Details of the ABAQUS numerical procedure are given in Appendix A, and a comparison between the numerical model and the analytical model of *Li and Rice* [1987] is given in Appendix B.

The Numerical Model

Approach

Our model for investigating the effects of nonlinear crustal rheology on periodic earthquake behavior assumes a very long vertical fault that penetrates a uniform, isotropic viscoelastic crust (Figure 2). At great distance from the fault a constant velocity directed parallel to the fault is specified; this velocity corresponds to the plate velocity. During an earthquake cycle the fault is locked, and at the end of the cycle it is abruptly moved to match the far-field plate displacement accumulated during that cycle.

We have determined the deformation and stresses in the crustal block during the great earthquake cycle by using the finite element code ABAQUS. This code accurately models three-dimensional, nonlinear, large deformation effects in solids, including heat transfer. The code features a robust element library comprising one-, two- and three-dimensional finite elements, linear and nonlinear material models, and accurate time-stepping algorithms and solution techniques for solving nonlinear equations. Details of the formulation and the numerical procedures are presented in Appendix A.

We employ eight-node linear isoparametric finite elements (or bricks) to represent the spatial variation of the displacement and stress fields (Figure 3) (Appendix A). With the linear isoparametric element, displacements vary linearly along the edges of each element. Strain and stress are determined at one integration point (stress and strain are constant within each element).

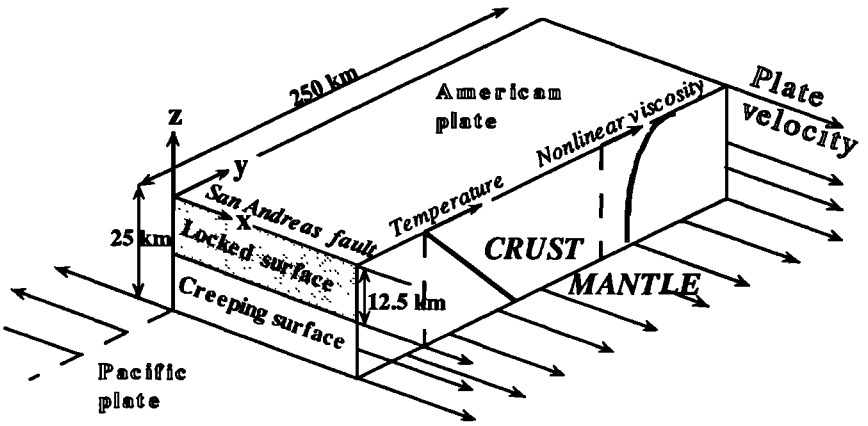

Figure 2. A model for crustal deformation during the earthquake cycle along the San Andreas fault, California. The model is an antiplane strain approximation for a long strike-slip fault. The crust is assumed to have a temperature-dependent, nonlinear, viscoelastic rheology. The locked part of the San Andreas fault is 12.5 km deep.

Model Parameters

Crustal and fault dimensions. The thickness of the California crust along the central San Andreas system ranges from 24 km to 26 km [*Oppenheimer and Eaton,* 1984; *Fuis and Mooney,* 1990], with 25 km as a representative thickness. Seismic activity along the San Andreas is mostly restricted to the upper 10–15 km, with local zones of deeper seismicity. It is generally accepted that the depth of seismicity corresponds to the depth of the portion of the San Andreas which slips during great earthquakes. We therefore use 25 km as the total crustal thickness and 12.5 km as the depth of the locked zone (Figure 2).

The assumption of a very long fault (Figure 2) reduces the problem to an antiplane condition. The deformation is restricted to a plane perpendicular to the fault and this deformation is defined in terms of a single unknown displacement component $u(y,z,t)$.The antiplane strain condition is enforced as described in Appendix A. We analyze the deformation within a crustal block that extends laterally from the fault at $y = 0$ to $y = 250$ km, and vertically from the ground at $z = 0$ to $z = -25$ km (Figures 2 and 3). The locked portion of the fault is the $x - z$ plane from $z = 0$ to $z = -12.5$ km. Three of the faces of the analyzed block slip at the constant fault-parallel horizontal velocity $v_p/2$, where v_p is the long-term slip rate along the fault. These faces are the downward continuation of the fault, from $z = -12.5$ km to $z = -25$ km, the base of the crustal block $z = -25$ km, and the far side of the block at $y = 250$ km (Figure 2). The fault itself, from $z = 0$ to $z = -12.5$ km, is locked (zero fault-parallel displacement) throughout the earthquake cycle except for a very brief period of time at the end of each cycle when the fault is abruptly displaced to catch up to the end at $y = 250$ km.

Long-term plate motion and loading history. The long-term slip rate along the San Andreas fault is about 35 mm yr^{-1} according to displaced Holocene features [*Lisowski et al.,* 1991]. Recent geodetic measurements indicate that the North American plate and the Pacific plate move at a relative velocity of up to 46 mm yr^{-1} [*Ward,* 1990], suggesting that part of the relative motion is accommodated by distributed deformation in a 200–400 km wide zone along the San Andreas fault. We consider only the component of the plate velocity that corresponds with slip along the San Andreas, i.e., $v_p = 35$ mm yr^{-1}.

Sieh et al. [1989] have shown that time intervals between great earthquakes in central California range from 44 to 332 years with the two most frequent intervals at about 250 and 50 years. Our numerical calculations are for an earthquake cycle time of 160 years, the same as in *Li and Rice* [1987], to facilitate benchmarking with their results (Appendix A).

Our model earthquake cycle is sketched in Figure 4. The constant velocity $v_p/2$ (17.5 mm yr^{-1}) is applied to all faces of the model except the locked portion of the fault (from $z = 0$ to $z = -12.5$ km) for the interseismic period of 160 years, yielding a total displacement of 2.8 m. Then the locked part of the fault is moved abruptly 2.8 m, and the cycle is repeated.

The calculations were carried out by stepping forward in time; approximately 20 time steps compose each cycle, with each run consisting of five to seven cycles. As solutions for the nonlinear rheology converge after three to four cycles we present below results for the fifth or sixth cycle.

Temperature. The thermal properties of the crust in the vicinity of the San Andreas fault are based on the analysis of surface heat flow data by *Lachenbruch and Sass* [1980]. They find that the mean surface heat flow along the San Andreas is 72 mW m^{-2}. They suggest that in spite of the wide scatter in the heat flow versus heat production data [*Lachenbruch and Sass,* Figure 10], the mantle heat flow in California may be comparable with that of the Basin and Range ($q_m = 58$ mW m^{-2}). Accordingly, we take $T_s = 10°$C, $q_s = 72$ mW m^{-2}, $q_m = 58$ mW m^{-2}, $k = 2.5$ W m^{-1}

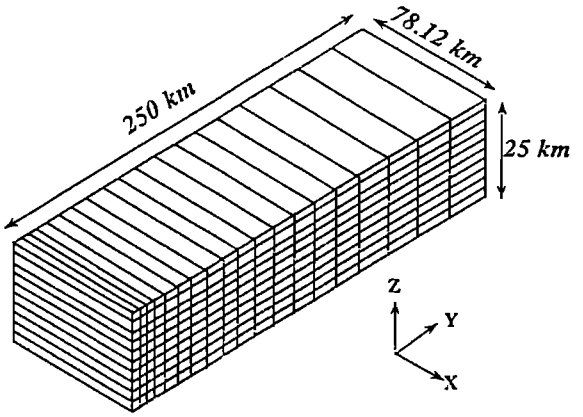

Figure 3. The NR2 mesh of elements used in the ABAQUS calculations. The mesh includes 440 nodes and 190 three-dimensional elements.

K^{-1} [*Lachenbruch and Sass*, 1980], and $h_r = 10$ km [*Turcotte and Schubert*, 1982] in equation (A7).

Rheology. We have assumed that the rheology of the entire crust can be represented by a single nonlinear, temperature-dependent viscoelastic law, as presented in equations (A5) and (A6). Then, the effective viscosity η when τ_{xy} is the only nonzero stress component is

$$\eta = \frac{(\tau_{xy})^{1-n} e^{\frac{Q}{RT}}}{(\sqrt{3})^{1+n} A_s}$$

The effective viscosities of six crustal rock types are plotted in Figure 5a for $\tau_{xy} = 1$ MPa, the temperature-depth profile equation (A7), and the values of A, n, and Q after *Kirby and Kronenberg* [1986] (Table 1). For these conditions, η ranges over 8 orders of magnitude (or more) from Westerly granite, the least viscous, to diabase, the most viscous (Figure 5a).

We carried out numerical simulations of the great earthquake cycle with the experimentally determined rheological properties of quartzite, quartz-diorite, and diabase. As shown below, only models with viscosity lower than the experimental viscosity of quartzite fit the field observations. Therefore the numerical results presented here are for five sets of rheological parameters which do not necessarily coincide with experimental parameters of a particular rock. These sets are as follows (Table 2): NR2D is identical to the experimental rheology of quartzite. NR2H and NR2J have the same Q as NR2D (quartzite) and values of A_s that are 100

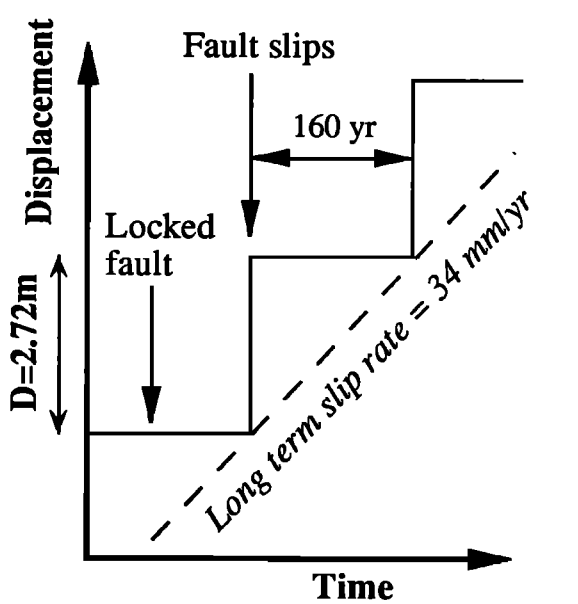

Figure 4. Loading history of the present model.

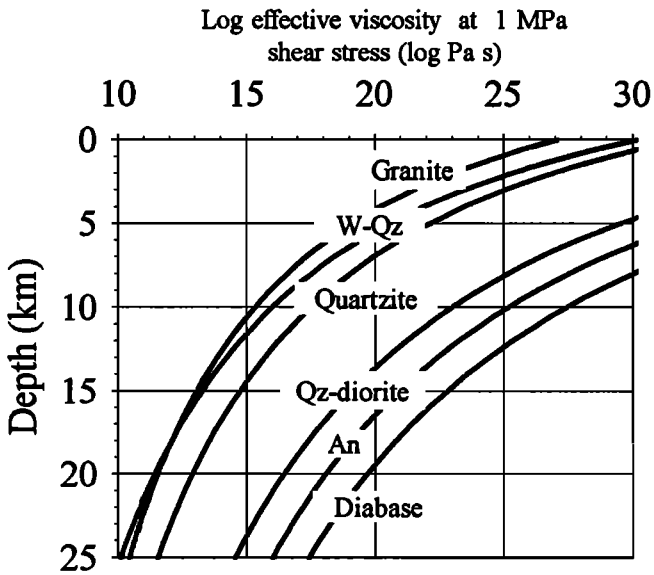

A.

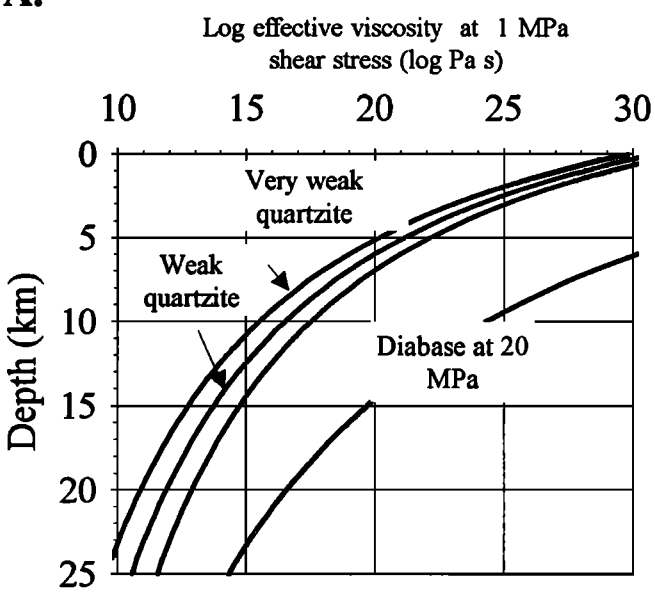

B.

Figure 5. The effective viscosity of (a) crustal rocks and (b) model materials versus crustal depth. The viscosity is calculated for the flow parameters given in Table 1 for rocks (laboratory parameters) and in Table 2 for model materials, the geothermal profile of California (see text), and a shear stress of 1 MPa.

Table 1. Nonlinear Viscosity Parameters of Crustal Rocks

Rock Type	A, $MPa^{-n}\ s^{-1}$	n	Q, $kJ\ mol^{-1}$
Quartzite (dry)	2.58×10^{-4}	2.4	155
Quartzite (wet)	6.79×10^{-3}	2.26	153
Westerly granite (wet/dry)	6.65×10^{-5}	2.73	127
Quartz-Diorite	1.29×10^{-3}	2.4	219
Anorthosite	3.16×10^{-4}	3.2	238
Diabase	2.00×10^{-4}	3.4	260

Selection from *Kirby and Kronenberg* [1986].

and 10 times larger, respectively, than the A_s value for quartzite. NR2I and NR2K have the same A_s as NR2J and values of Q which are 0.9 and 1.1 times the value of Q for NR2J, respectively. All sets of rheological parameters have the same value of n as quartzite.

The effective viscosities of these five rheological parameter sets are plotted in Figure 5b for the same temperature distribution and shear stress as used in calculating η for the laboratory-determined rheological parameters (Figure 5a). In general, η(NR2D)$\approx$ η(NR2I) and η(NR2H)$\approx$ η(NR2K); thus numerical solutions for these two pairs of rheological models turn out to be approximately the same. These results imply that a factor of 10 change in the multiplication factor A_s is equivalent to about a 10% change in the activation energy Q.

Below we present the results for the rheological parameters NR2D and NR2H, and we also discuss the results for NR2J. For convenience in recognition we rename the rheological models: NR2D is termed "quartzite," NR2J is termed "weak quartzite" and NR2H is termed "very weak quartzite."

Results

The model results presented here are for the rheological parameter sets "quartzite" and "very weak quartzite" (Table 2) as discussed above. The results include the vertical and horizontal distributions of fault-parallel velocity, fault-parallel displacement, and fault-parallel shear stress during the earthquake cycle. The velocity, displacement, and shear stress are calculated at five times during the cycle (usually 10, 40 or 50, 72, 121, and 156 or 160 years after the earthquake) and are plotted in Figures 6–9.

Fault-Parallel Velocity

Variations in the fault-parallel velocity during the earthquake cycle are shown in Figure 6a for the "very weak quartzite" model. Surface velocity is plotted as a function of distance from the fault at several times during the earthquake cycle. The spatial variations in surface velocity occur within an $\approx$150-km-wide zone on either side of the fault. During a post-seismic period of $\approx$50 years, the surface velocity several tens of kilometers away from the fault exceeds the long-term plate velocity. On the other hand, during a preseismic period of $\approx$40 years, the surface velocity at distances up to $\approx$50 km from the fault is significantly below the plate velocity. For example, the velocity at a distance of $\approx$30 km away from the fault drops from 1.65 times the plate velocity 10 years after the earthquake to about 0.45 times the plate velocity 156 years after the earthquake (i.e., 4 years before the next earthquake). Thus the variations in surface velocity by this model display a profound postseismic transient mode.

Figure 7a shows the depth distribution of the fault-parallel velocity at a distance of 3.8 km from the fault and at several times in the earthquake cycle for the "very weak quartzite" model. The velocity variations with depth and time during the postseismic transient are particularly large below about 10 km depth in the relatively low viscosity lower crust. For example, the velocity at a depth of about 18 km changes from $\approx$1.4 times the plate velocity 10 years after the earthquake to $\approx$0.3 times the plate velocity 156 years after the earthquake. From the surface to $\approx$10 km depth, the upper crust moves at an approximately constant velocity at any stage of the earthquake cycle. Prior to the earthquake, the velocity decreases approximately linearly from the plate velocity (17.5 mm yr^{-1}) at 25 km depth to about 0.07 times the plate velocity at 15 km depth, while the crust above 15 km moves at a relatively constant velocity of 0.05–0.07 times the plate velocity. Thus the upper crust is partially decoupled from the mantle by flow within the lower crust.

Table 2. Nonlinear Viscosity Parameters of the Models Studied in This Paper (Equations (A5) and (A6))

Model Name on ABAQUS (Model Name Used Here)	A_s, $MPa^{-n}\ s^{-1}$	n	Q, $kJ\ mol^{-1}$	Comments
NR2D ("Quartzite")	2.58×10^{-4}	2.4	155	quartzite rheology
NR2H ("Very weak quartzite")	2.58×10^{-2}	2.4	155	0.01 times quartzite viscosity
NR2I	2.58×10^{-3}	2.4	140	
NR2J ("Weak quartzite")	2.58×10^{-3}	2.4	155	0.1 times quartzite viscosity
NR2K	2.58×10^{-3}	2.4	170	

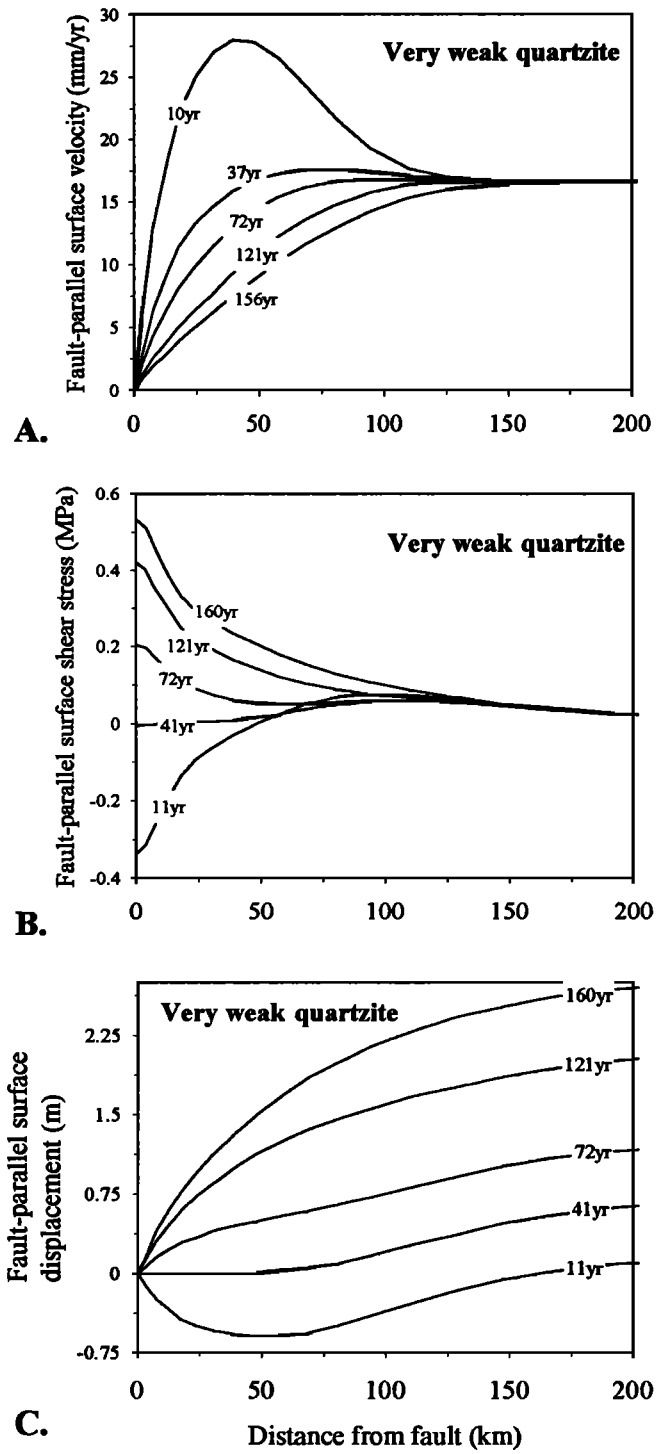

Figure 6. (a) Fault-parallel surface velocity, (b) surface shear stress, and (c) fault-parallel surface displacement versus distance from the fault for model NR2H ("very weak quartzite" in Table 2). The shear stress does not include the ambient stress. The results are for five times since the last great earthquake.

Temporal variations in fault-parallel surface velocity during the earthquake cycle are rather different for the "quartzite" model (Figure 8a). The velocity variations with time are relatively small; for example, at a distance of ≈25 km away from the fault, the surface velocity drops from ≈0.85 times the plate velocity 10 years after the earthquake to ≈0.7 times the plate velocity 4 years before the next earthquake (Figure 8a). The zone of deformation in this model is ≈75 km wide, approximately half of the deformation zone width in the "very weak quartzite" model.

Figure 9a shows the depth distribution of the fault-parallel velocity at a distance of 3.8 km from the fault and at several times in the earthquake cycle for the "quartzite" model. Temporal variations in velocity are relatively small at all depths. The fault-parallel velocity decreases approximately linearly from the plate velocity (17.5 mm yr^{-1}) at 25 km depth to ≈0.2 times the plate velocity at ≈10 km depth; the crust above 10 km moves at the roughly constant velocity of 0.2 times the plate velocity.

Fault-Parallel Displacement

The displacements for models NR2H ("very weak quartzite") and NR2D ("quartzite") are shown in Figures 6c and 8c, respectively, as a function of distance from the fault plane at several times during the earthquake cycle. As the fault is locked during the entire cycle (excluding the short event of the earthquake), the fault is the reference point for the displacements. The displacement at the fault is constant and zero, and the displacement at distance of 250 km at a given time is the integrated plate velocity since the earthquake. For the quartzite rheology (Figure 8c), spatial variations in fault-parallel surface displacement are confined to distances < 75 km on either side of the fault, but for "very weak quartzite" (Figure 6c) the variations extend farther from the fault to distances of about ≈200 km.

During an early postseismic period (≈40 years after the earthquake for the weakened quartzite rheology, Figure 6c, and a somewhat shorter time for the quartzite rheology, Figure 8c), the displacement near the fault is inverted from the sense of the long-term or far-field displacement; i.e., there is left-lateral displacement in contrast to the long-term right-lateral slip along the San Andreas fault. The inverted displacement during the early postseismic period reflects the velocity deficit near the fault during the late stages of the earthquake cycle. When the earthquake occurs, material close to the fault plane, whose fault-parallel velocity and displacement have been retarded by the locked fault during most of the earthquake cycle (compare times of 160 and 11 years in Figures 6c and 8c), moves ahead of material farther from the fault plane. The late stage velocity deficit is smaller and concentrated closer to the fault for the stronger rheology (compare Figures 6a and 8a), making the inverted displacement smaller and confined nearer the fault. Thus the inverted sense of displacement reflects the viscoelastic character of the model. Note that the fault-parallel velocity itself is always in the right-lateral sense and not inverted at any stage of the earthquake cycle.

Figures 7c and 9c show the variations with depth, at several times during the earthquake cycle, of the fault-parallel displacement at 3.8 km from the fault for the

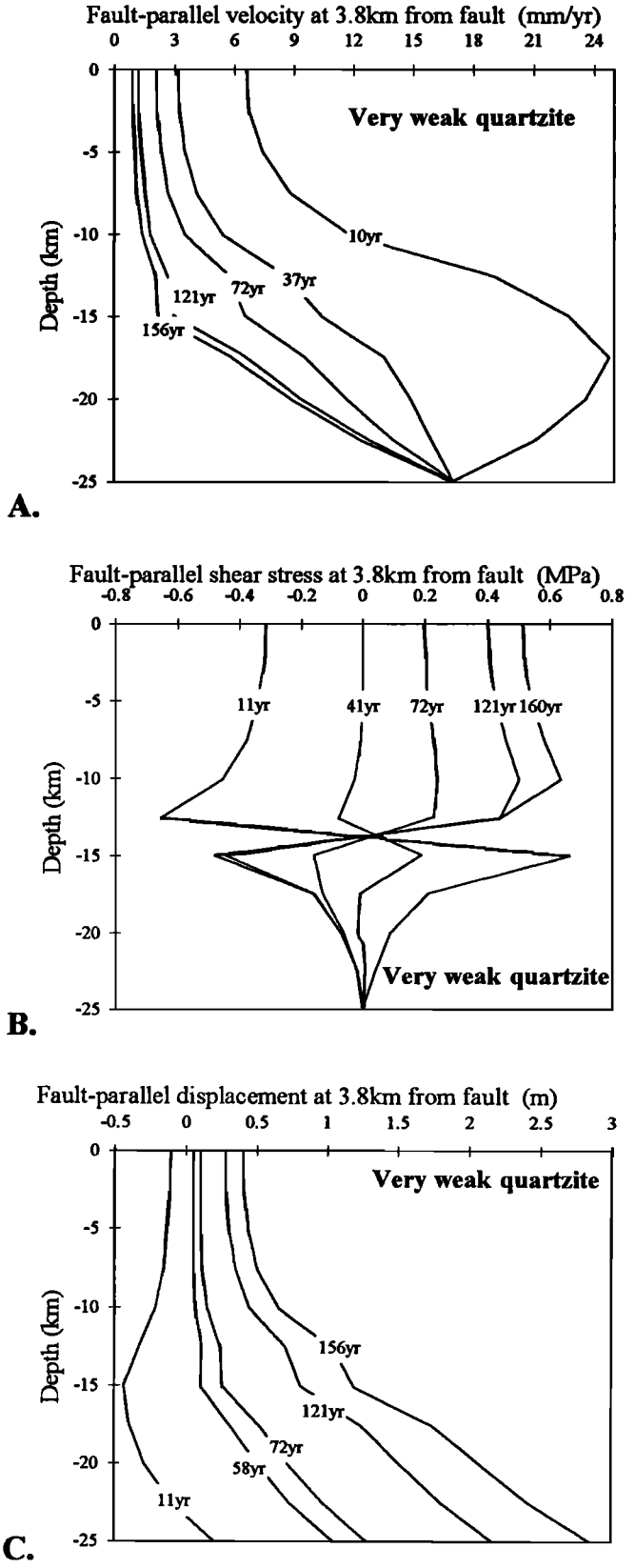

Figure 7. (a) Fault-parallel velocity, (b) shear stress, and (c) fault-parallel displacement versus depth for model NR2H ("very weak quartzite" in Table 2), at a distance of 3.8 km from the San Andreas fault. Ambient stresses are not included. The results are shown for five elapsed times since the last great earthquake.

"very weak quartzite" and "quartzite" models, respectively. The left-lateral displacement early in the earthquake cycle occurs over the entire thickness of the crust for both rheologies. The upper ≈10 km of the crust moves relatively rigidly in contrast to the strong decoupling that occurs within the lower ≈15 km of the crust for both the quartzite and weakened quartzite rheologies.

Fault-Parallel Shear Stress

The fault-parallel surface shear stress is plotted in Figures 6b and 8b as a function of distance from the fault at several times during the earthquake cycle for the weakened quartzite and quartzite rheologies, respectively. The shear stress in these figures indicates only the deviation from the ambient tectonic stress; the latter might be significantly larger. The ambient stress cannot be calculated in the present modeling as the strength of the San Andreas fault was not specified.

The shear stress variations throughout the earthquake cycle increase with proximity to the fault (Figures 6b and 8b). The variations in shear stress that are earthquake related are the difference between the shear stress just before the earthquake (the 160-year curves in Figures 6b and 8b), and the shear stress a short period after the earthquake (the 11-year curves in Figures 6b and 8b). Figure 6b (weakened quartzite) indicates that the shear stress next to the fault is 0.53 MPa at the end of the cycle and −0.33 MPa at 11 years after the earthquake; thus the stress change is 0.86 MPa. Similarly, Figure 8b indicates a stress change of 1.33 MPa (0.93 MPa before and −0.3 MPa 11 years after the earthquake).

The shear stress also changes sign during the earthquake, from right-lateral shear before the earthquake (the 41- to 160-year curves in Figure 6b) to left-lateral shear after the earthquake (the 11- to 41-year curves in Figure 6b). As the ambient shear stress is unknown, it is not clear if this sign change is sufficient to significantly affect the state of stress in the crust. The right-lateral shear stress during the late stages of the earthquake cycle corresponds to right lateral displacement (41- to 160-year curves in Figure 6c), whereas the left-lateral shear during the early stages of the earthquake cycle corresponds to left-lateral displacement (11- to 41-year curves in Figure 6b).

Figures 7b and 9b show that shear stresses at 3.8 km from the fault are relatively constant with depth in the upper ≈10 km of the crust at all stages of the earthquake cycle. Below ≈10–15 km there is a reversal in the sign of the shear stress; while left-lateral shear prevails in the upper crust during the first ≈40 years of the cycle, right-lateral shear prevails in the lower crust for the same period and vice versa for the later stages of the cycle.

Field Observations and Model Predictions

We compare the results of the model calculations with three sets of geodetic data for the San Andreas system

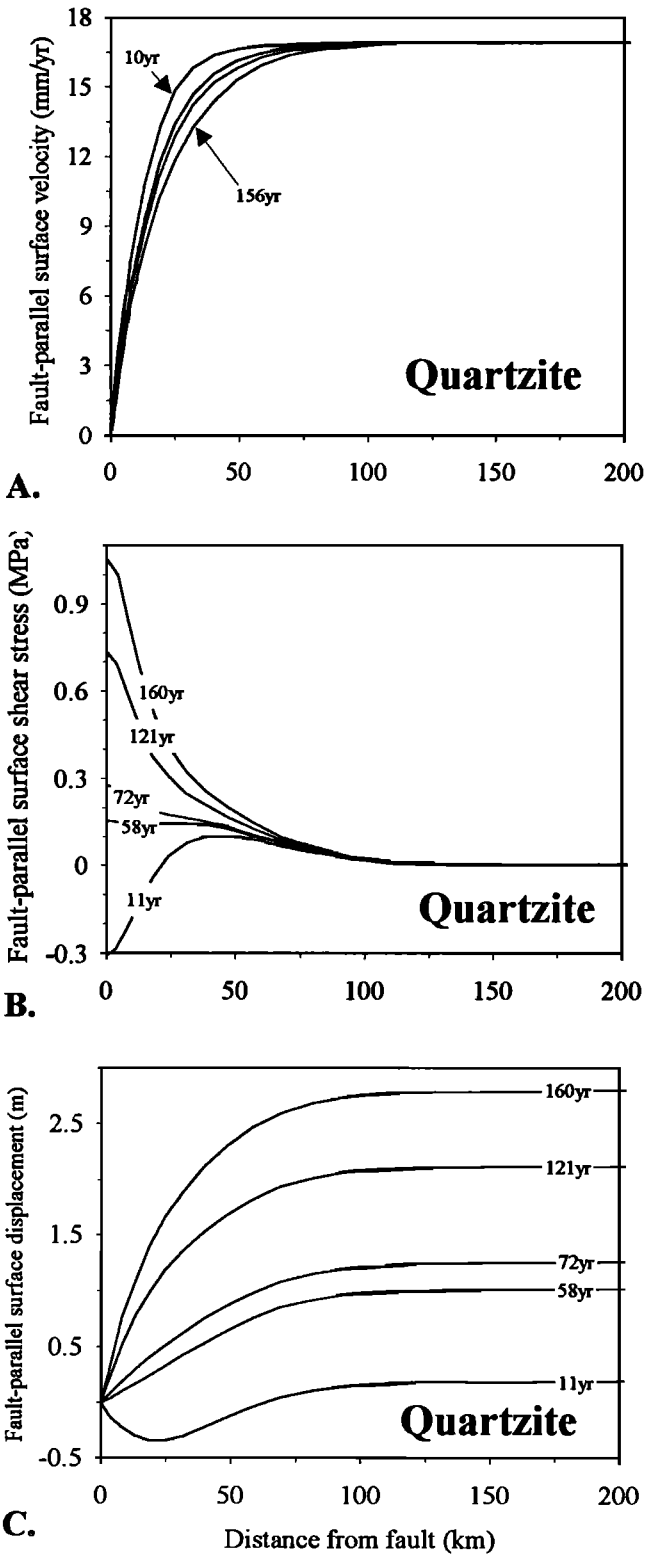

Figure 8. Similar to Figure 6, for model NR2D ("quartzite" model in Table 2).

(Figure 10). We use the fault-parallel velocities measured in northern California [*Prescott and Yu*, 1986], the fault-parallel velocities in central California [*Lisowski et al.*, 1991], and the rate of shear strain for various sites along the San Andreas system [*Thatcher*, 1983]. In this selection of geodetic data sets we follow the work of *Li and Rice* [1987].

Fault-Parallel Velocity

We first compare the numerical results with the measured fault-parallel velocities in the central Transverse Ranges [*Lisowski et al.*, 1991] and north of San Fran-

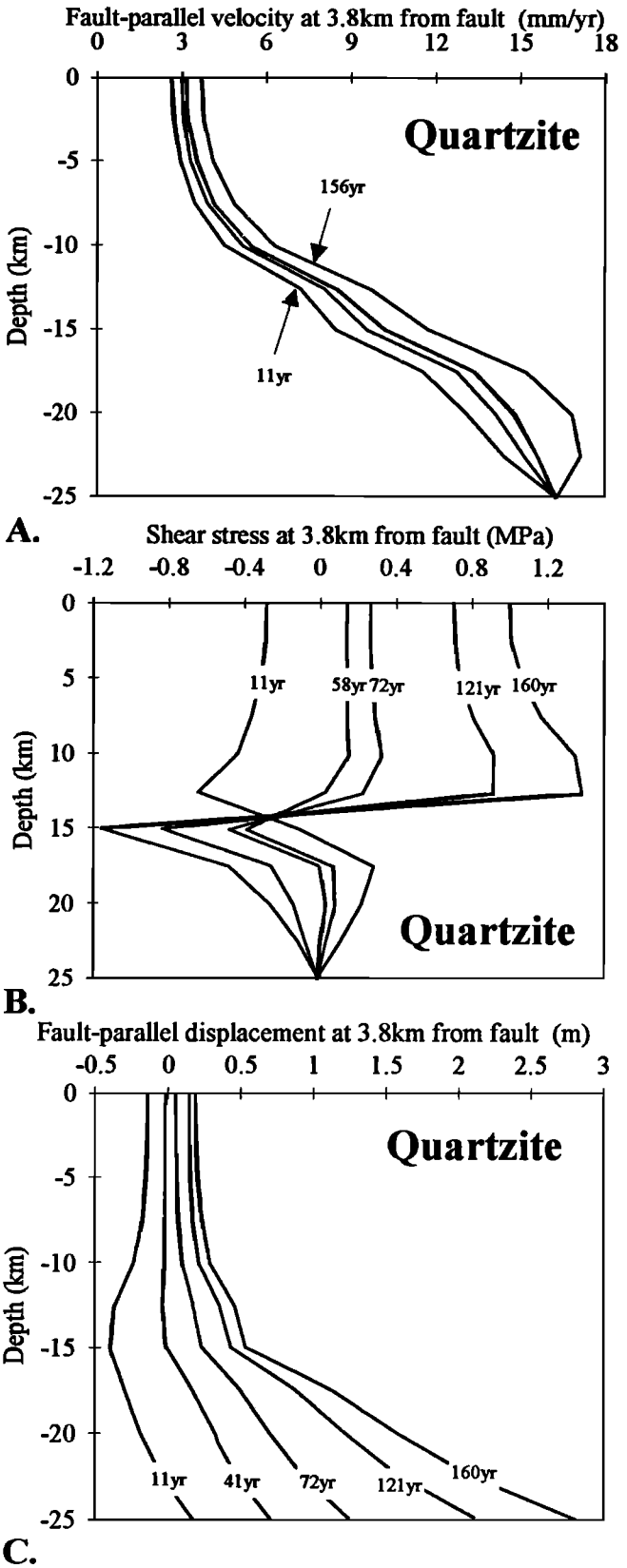

Figure 9. Similar to Figure 7, for model NR2D ("quartzite" model in Table 2).

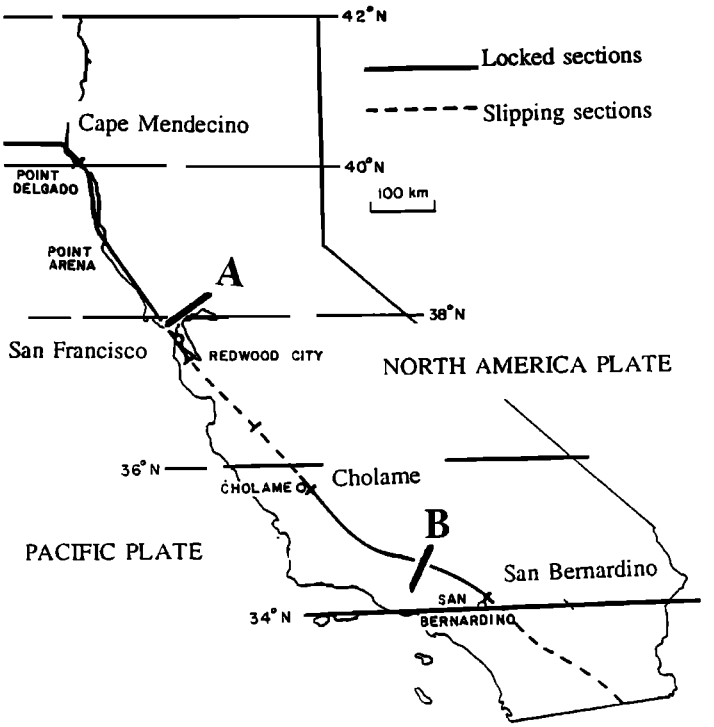

Figure 10. Simplified map of the San Andreas fault with the two locked segments analyzed here [after *Turcotte and Schubert*, 1982]. The calculated fault-parallel velocities are compared with geodetically determined velocities at the locations on the map. Profile A, north of San Francisco Bay, velocities after the 1906 San Francisco earthquake [*Prescott and Yu*, 1986]; profile B, central Transverse Ranges, velocities after the 1857 Fort Tejon earthquake [*Lisowski et al.*, 1991].

cisco Bay [*Prescott and Yu*, 1986]. The models are "quartzite," "weak quartzite," and "very weak quartzite" of Table 2.

The fault-parallel velocities in the region north of San Francisco Bay were measured during 1972–1982 by *Prescott and Yu* [1986] (Figure 11). They regarded these as steady state velocities since they were essentially constant during the survey period some 70 years after the 1906 San Francisco earthquake. The measurements are consistent with a monotonic increase in the magnitude of the velocity with distance from the fault, with the velocity approaching an asymptotic plate tectonic speed at distances greater than about 50 km from the fault. Local velocity deviations have been attributed to features such as The Geysers thermal anomaly [*Prescott and Yu*, 1986]. *Prescott and Yu* [1986] showed that the data in Figure 11 could be matched by deformation in an elastic half-space with an appropriate distribution of dislocations. Several of the dislocations in their set extend from depths of 10 km to infinity (see discussion).

Figure 11 also shows the fault-parallel surface velocities versus distance from the fault for the three models of "quartzite," "weak quartzite," and "very weak quartzite" at 72 years after the earthquake. The three model curves all fit the observations which have relatively large uncertainties. An interesting feature of this plot is the coincidence of the velocities for models "quartzite" and "weak quartzite" even though these models differ by a factor of 10 in viscosity. The higher-viscosity model ("quartzite") has relatively little variation in fault-parallel surface velocity with time during the earthquake cycle (Figure 8a). The model with lower viscosity ("weak quartzite") has a greater time variation in fault-parallel surface velocity (see Figure 6a for the "very weak quartzite" model); the low-viscosity model evolves from a high velocity postseismic state to a lower-velocity preseismic state. At 72 years after the earthquake the intermediate velocity state of the low-viscosity model happens to coincide with that of the high-viscosity model.

The observations of fault-parallel surface velocities in the central Transverse Ranges compiled by *Lisowski et al.* [1991] are shown in Figure 12. It is assumed that these velocities are related to the 1857 Fort-Tejon earthquake. Figure 12 also displays the model velocities calculated 121 years after the earthquake. The field data are fit well by the velocities of the low viscosity models NR2J and "very weak quartzite"; the viscoelastic model of *Li and Rice* [1987] also provides a good match to the observations.

Figures 11 and 12 emphasize that models with different crustal viscosities yield different velocity distributions. These distributions could be distinguishable by geodetic observations even a long time after the last great earthquake, for example, 121 years in Figure 12. These velocity differences that are associated with different viscosities probably reflect the degree of coupling between the lower and upper crust. In our model, the base of the crust is subjected to a constant plate veloc-

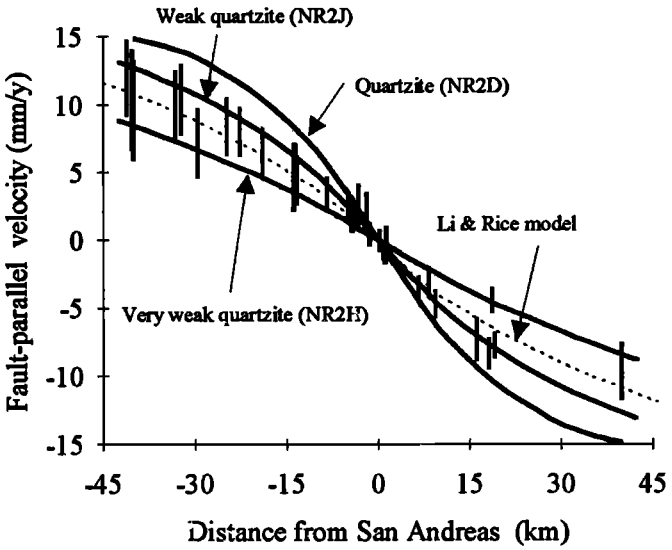

Figure 11. Fault-parallel surface velocity along profile A in Figure 10. Vertical bars (2 standard deviations in length) indicate the geodetic velocities for the period 1973–1984 as determined by *Prescott and Yu* [1986]. Solid curves are the calculated velocities 72 years after the great earthquake for models NR2D ("quartzite"), NR2J ("weak quartzite"), and NR2H ("very weak quartzite"). The curves for NR2D and NR2J coincide (see text).

ity of $v_p/2$. The effective viscosity of the model crust at 1 MPa shear stress varies strongly with depth, from approximately 10^{30} Pa s at the surface to $\approx 10^{11}$ Pa s at the base (for the "quartzite" model). A lower crust with such a low viscosity cannot apply large shear stresses to the upper crust (Figures 7b and 9b); it essentially generates a zone of partial decoupling between the upper crust and the mantle.

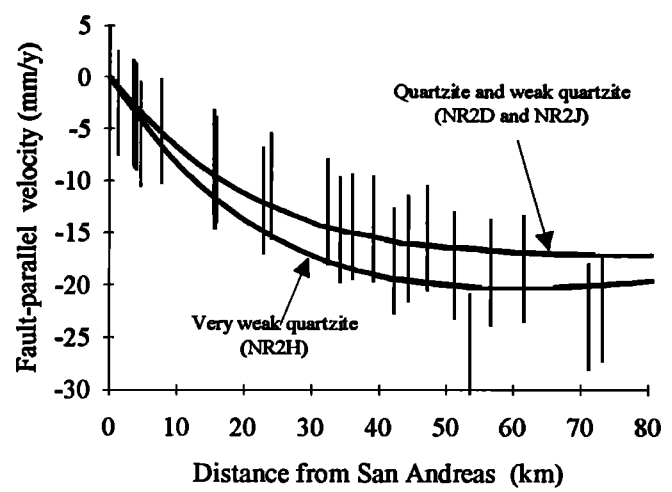

Figure 12. Fault-parallel surface velocities on both sides of the San Andreas fault along profile B in Figure 10. Vertical bars (two standard deviations in length) indicate the geodetic velocities as presented by *Lisowski et al.* [1991]. Solid curves are the calculated velocities 123 years after the great earthquake for models NR2D ("quartzite"), NR2J ("weak quartzite"), and NR2H ("very weak quartzite").

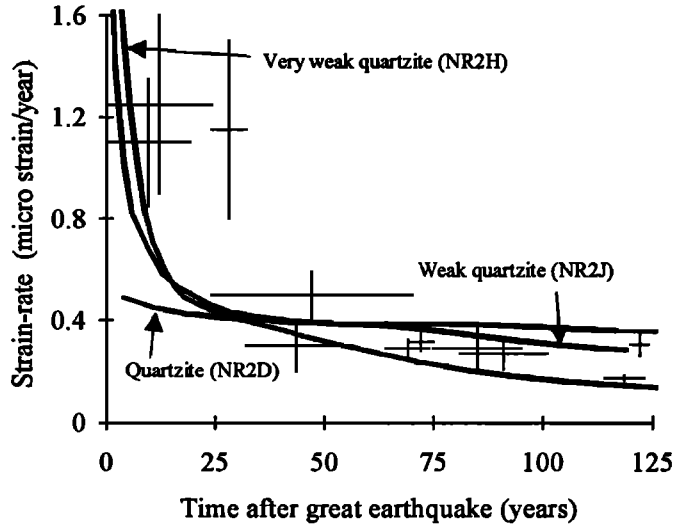

Figure 13. Rates of fault-parallel shear strain near the San Andreas fault for various times after the great earthquake. Vertical and horizontal bars (2 standard deviations in length) are the strain rates estimated from geodetic data by *Thatcher* [1983]. Solid curves are the calculated velocities 123 years after the great earthquake, for models NR2D ("quartzite"), NR2J ("weak quartzite"), and NR2H ("very weak quartzite").

Rate of Shear Strain

Thatcher [1983] calculated the shear strain rates parallel to the San Andreas fault ($\dot{\gamma}_{xy}$ in the present convention), from geodetic measurements at different stages of the earthquake cycle. Figure 13 displays these geodetic strain rates versus elapsed time since the last major earthquake. After about 50 years following the earthquake, the measured strain rates approach an approximately constant value of 0.3×10^{-6} yr^{-1}. During the transient stage of $\approx$50 years following the earthquake, the measured strain rates are highly variable and have large uncertainties.

Figure 13 also shows $\dot{\gamma}_{xy}$ predicted by "quartzite," "weak quartzite," and "very weak quartzite" models; these rates were calculated for the ground surface at a distance of 6 km away from the fault. For periods of more than about 50 years after the earthquake, the three models fit the measurements about equally well. However, the situation is different for the first 50 years after the earthquake during which none of the models provides a good fit to the measured strain rate. Models "weak quartzite" and "very weak quartzite" fit the data better than the "quartzite" model (Figure 13), in accord with the above deductions for the fault-parallel velocities (Figures 11 and 12).

Summary: Comparison of Observations and Predictions

The good agreement shown between geodetic observations and predictions of the "weak quartzite" and "very weak quartzite" models (Figures 11–13) is significant for several reasons. First, the model parameters represent thermal and mechanical properties of the

crust in the vicinity of the San Andreas fault and the agreement is found without parameter fitting and without local, ad hoc modifications. Second, the same model fits, in general, the velocity observations in several regions, each in a different stage of the earthquake cycle. Third, the comparison between predicted and observed surface velocities indicates some decoupling within the lower crust. In particular, the estimated in situ viscosity of the lower crustal rocks near the San Andreas is similar to the viscosity of one of the less viscous crustal rocks tested in laboratory experiments (i.e., Westerly granite, see Figure 5).

Discussion

Composition of the Lower Crust and in Situ Rheology

The seismic structure of the lithosphere and the composition of its lower crust in central and southern California were recently examined by *Fuis and Mooney* [1990]. Their profile for central California [*Fuis and Mooney,* 1990, Figure 8.5] shows that the seismic velocity exceeds 6.0 km s^{-1} (approximately granite velocity) at a depth of 5 km in the Salinian block west of the San Andreas (Santa Cruz Mountains/Gabilan Range) and at depth of 15 km in the Diablo Range, east of the San Andreas. Detailed velocity-depth profiles for these two regions are presented in Figure 14. For the Salinian block *Fuis and Mooney* [1990, p. 216] suggested two possible compositions of layer 4, at depth of 10 to 25 km (Figure 14a): "... gneiss of intermediate [diorite] composition... [or] in an alternative model, where middle and lower crust are separated as layers 4a and 4b, layer 4b may be reasonably interpreted as gabbro" (Figure 14a). For the Diablo Range, *Fuis and Mooney* [1990] showed that the velocities of the lower crust at depths of 15–29 km are compatible with a gabbroic composition (Figure 14b). The structure in southern California is more complicated and data are more limited. For the Peninsular Ranges, the seismic velocity is 5.9 km s^{-1} to a depth of 8 km and 6.8 km s^{-1} from 8 km to 26 km [*Fuis and Mooney,* 1990]. Although *Fuis and Mooney* [1990] mention several different interpretations of the seismic velocity profiles, none of the alternate models include a granitic composition for the lower crust.

We showed that the geodetic observations along the San Andreas can be matched only if the rheology of the lower crust is weaker than the experimentally determined rheology of quartzite (or similar to the rheology of a less viscous rock such as Westerly granite). The effective viscosities of our "quartzite" to "very weak quartzite" models are 3–6 orders of magnitude less than the effective viscosities of quartz-diorite (intermediate) and diabase (Figure 4b), the rocks anticipated in the lower crust.

This discrepancy is probably related to the intrinsic difference between in situ viscosity and laboratory viscosity due to a few reasons. First, the strain rates in most laboratory tests range from 10^{-6} s^{-1} to 10^{-8} s^{-1}, whereas the regional strain rates in the field (and in the present model) are 10^{-14} to 10^{-15} s^{-1} (strain rates that are comparable to the experimental strain rates could last for periods of days after the earthquake at the immediate proximity of the fault). The second reason is related to the size of the sample. The lower crust could include narrow shear zones that accommodate large strain and broad zones of relatively small strain. Laboratory measurements of small samples cannot account for the large-scale complexity of such systems. A third option is related to the deformation mechanisms active in laboratory testing of lower crustal rocks. For example, pressure solution creep cannot be studied experimentally due to its slow rate, yet it might be effective under crustal conditions.

The estimated effective viscosity of the lower crust is very low, and such low-viscosity could lead to decoupling between the mantle and the crust and to seismic attenuation. This low viscosity layer probably does not affect postglacial rebound analyses because of the wavelength differences: the postglacial rebound requires flow on continental scale which is accommodated primarily in the mantle. Geodetic observations of earthquake displacement are a good way to estimate the viscosity of the lower crust due to the similarity in relaxation time and length scales.

Limitations of the Model

While the present model provides good fits to field observations of earthquake related deformation along the San Andreas fault (Figures 11–13), so do previous models with dislocations in elastic layers or linear viscoelastic layers [e.g., *Prescott and Yu,* 1986; *Lisowski et al.,* 1991; *Li and Rice,* 1987]. Models with dislocations in elastic layers frequently fit the geodetic observations by employing "very deep" dislocations that may extend thousands of kilometers in depth for the elastic half-space calculation or by using ad hoc sets of shallow dislocations that generate pseudo-viscous deformations. Some of the linear viscoelastic models are based on the generalized Elsasser approximation [*Li and Rice,* 1987]. The fitting of the geodetic data in this approximation is obtained by adjusting a central parameter that is not measurable either in situ or in the laboratory (Appendix B).

Crustal rocks, however, have a nonlinear and temperature-dependent rheology that is incorporated into the present modeling. Yet, while the present model examines the complete range of the nonlinear viscosity of crustal rocks, it is restricted in other parameters. These parameters are crustal thickness (25 km); depth of locked fault (12.5 km); period of earthquake cycle (160 years); slip rate (35 mm/yr); constant velocity at the base of the crust and below the fault; earthquake magnitude (great, $M > 8$); shear modulus /Poisson's ratio (35 GPa/0.25); fault geometry (vertical, long, two-dimensional, antiplane); constant crustal lithology and constant thermal parameters. These parameters are not necessarily constant, and the effect of their variations cannot be easily evaluated. We regard the investigation of these parameters as a task for future study.

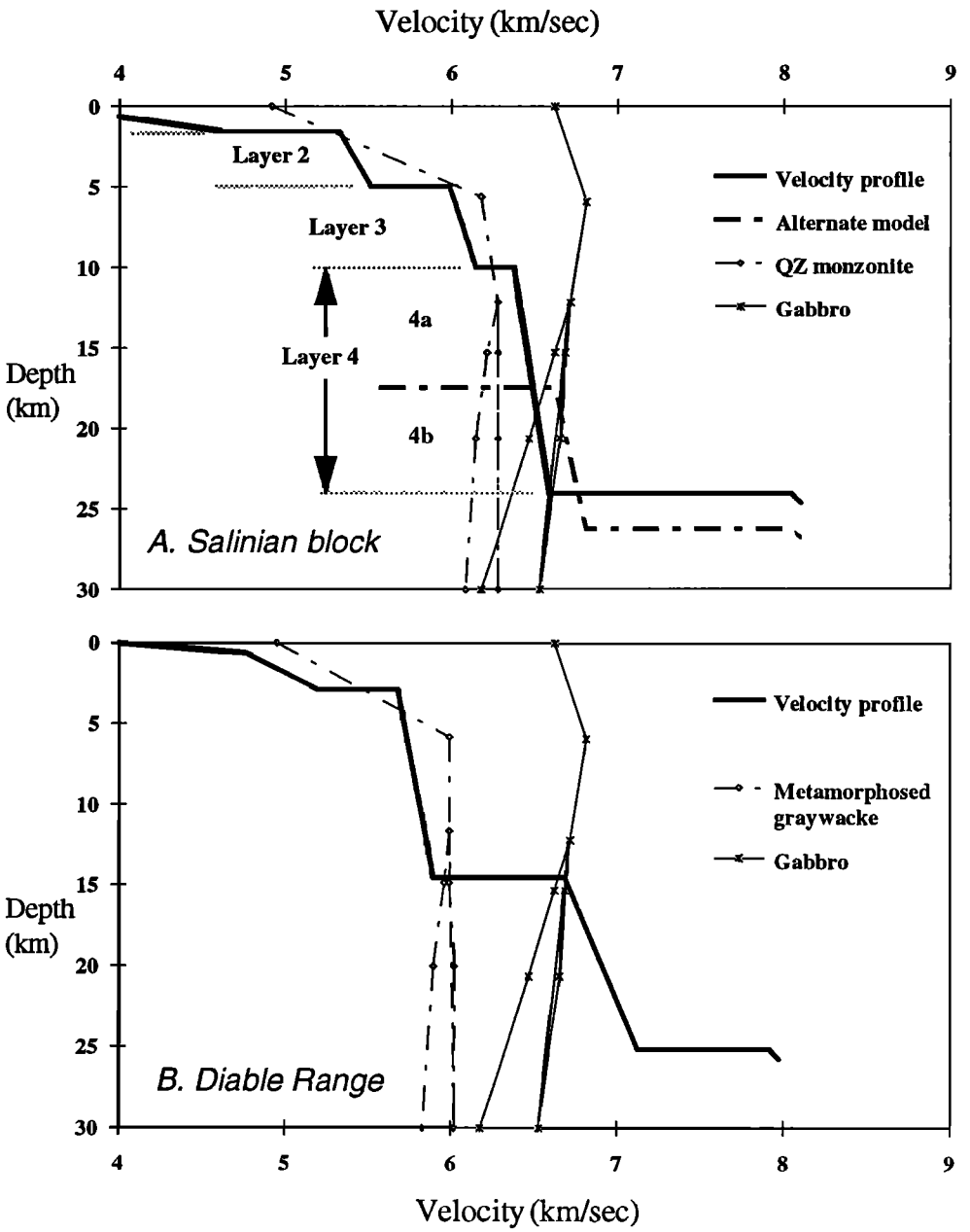

Figure 14. Velocity-depth curves for central California. (a) Salinian block. (b) Diablo Range. Heavy lines are seismic velocities; light lines with symbols are velocities from laboratory measurements (two different geotherms were assumed below 10 km) [after *Fuis and Mooney* 1990, Figure 8.5].

Conclusions

We analyzed the cycles of great California earthquakes by using finite element computations for a temperature-dependent, nonlinear viscoelastic crust. The known crustal thickness and crustal temperature for California and the slip rate of the San Andreas fault were used in the computations. The analysis leads to the following conclusions:

1. The viscous rheology of the crust strongly affects the transient behavior of large earthquakes. Models with a rheology similar to granite or quartzite display profound transient stages in the velocity, displacement, and stress fields (Figures 6–9). On the other hand, models with stiff diabase-like rheology display insignificant transient stages, and in this respect, models with diabase rheology resemble elastic models. Since large earthquakes display transient behavior, reflected in the aftershock activity and the postseismic deformation, elastic models of the crust are probably inadequate to describe the earthquake cycle.

2. The models which best fit the geodetic data of California have rheological parameters that are similar to the experimentally determined values of Westerly

granite and wet quartzite; these are the least viscous of the crustal rocks considered by *Kirby and Kronenberg* [1986]. Since the lower crust of California is more mafic then Westerly granite (diorite to gabbro composition [*Fuis and Mooney,* 1990]), we conclude that the in situ viscosity of crustal rocks is significantly smaller than the viscosity determined in the laboratory measurements. We estimate that the in situ effective viscosity is 10^{-2} to 10^{-6} of the viscosity inferred from laboratory measurements.

3. The model calculations indicate that the effective viscosity at the base of the crust might be as low as 10^{11} Pa s. In the present analysis the base of the crust moves at the uniform plate velocity assuming perfect coupling between the mantle and the crustal base (Figure 2). However, since the lower crust cannot support high shear stresses, the basal plate motion is not fully transmitted to the upper crust, and a zone of partial, transient decoupling develops within the lower crust (Figures 7b and 7c). Some of the geodetic observations made ≈70 to 120 years after a major earthquake, which is relatively late in the cycle, are in agreement with such decoupling (Figures 11 and 12).

4. The models that better fit the geodetic data (Figures 11–13) display transient stages that include large spatial variations in the displacements, velocities and shear stresses (Figures 6 and 7). These spatial changes occur within a deformation zone along the fault; the width of this zone depends on crustal viscosity. It is about 75 km (on either side of the fault) for the "quartzite" model (Figure 8), and it is more than 150 km for the "very weak quartzite" model Figure 6). These widths are significantly larger than the 50 km distance calculated for a model with diabase rheology (not shown here). Further, these widths are constant during the earthquake cycle, in contrast to the widening of the deformation zone predicted by *Thatcher* [1983]. The widths of the deformation zones in our calculations suggest that geodetic data should be measured over distances of 200 km from the San Andreas fault to adequately represent the transient deformation.

5. The transient stage of 50 years for the least viscous model ("very weak quartzite" in Figures 6 and 7) displays some new features not predicted by elastic models. First, the surface velocity away from the fault exceeds the long-term plate velocity by as much as 65% (Figures 6a and 7a). Second, the sense of the fault-parallel displacement near the fault is inverted with respect to the long-term and far-field displacement; i.e., transient left-lateral displacement is predicted in contrast to the long-term right-lateral slip of the entire fault system (Figures 6c and 7c). Third, the fault-parallel shear stress is also inverted with respect to the long-term shear (note the left-lateral shear in Figures 6b and 7b).

Appendix A: Numerical Methods

Our model assumes a very long vertical fault that penetrates a uniform, isotropic viscoelastic crust (Figure 2). At great distance from the fault a constant velocity directed parallel to the fault is specified. During an earthquake cycle the fault is locked, and at the end of the cycle it is abruptly moved to match the far-field plate displacement accumulated during that cycle. Under such assumptions the problem can be modeled as antiplane strain with the time-varying displacement field of the form

$$u = u(y,z,t), \quad v = 0, \quad w = 0 \tag{A1}$$

where t is time, x is the coordinate directed horizontally along the fault, y is the horizontal coordinate normal to the fault, z is the vertical coordinate (Figure 2), and u, v, w are displacements along x, y, z. For antiplane strain the strain rates can be written as

$$\dot{\epsilon}_x = 0, \ \dot{\epsilon}_y = 0, \ \dot{\epsilon}_z = 0, \ \dot{\gamma}_{xy} = \frac{1}{2}\frac{\partial^2 u}{\partial y \partial t}, \quad \dot{\gamma}_{xz} = \frac{1}{2}\frac{\partial^2 u}{\partial z \partial t}, \ \dot{\gamma}_{yz} = 0. \tag{A2}$$

The only nonzero strain rate components are the components $\dot{\gamma}_{xy}$ and $\dot{\gamma}_{xz}$. From the elastic relations and the assumption of additivity of the elastic and viscous strain rates (denoted by superscripts v) we obtain the constitutive relations for our problem

$$\dot{\gamma}_{xy} = \frac{1}{2G}\dot{\tau}_{xy} + \dot{\gamma}^v_{xy}, \ \dot{\gamma}_{xz} = \frac{1}{2G}\dot{\tau}_{xz} + \dot{\gamma}^v_{xz}. \tag{A3}$$

Equations (A2) and (A3) must be supplemented with the equilibrium equations for the shear stresses τ_{xy} and τ_{xz}

$$\frac{\partial \tau_{xy}}{\partial y} + \frac{\partial \tau_{xz}}{\partial z} = 0 \tag{A4}$$

and the relationship between the viscous strain rates and the shear stresses

$$\dot{\gamma}^v_{xy} = \frac{3}{2}\bar{\tau}^{n-1} A_s e^{-Q/RT} \tau_{xy}, \tag{A5}$$

$$\dot{\gamma}^v_{xz} = \frac{3}{2}\bar{\tau}^{n-1} A_s e^{-Q/RT} \tau_{xz}, \tag{A6}$$

where $\bar{\tau} = \sqrt{3}\left(\tau^2_{xy} + \tau^2_{xz}\right)^{1/2}$, A_s and n are rheological constants, Q is activation energy, R is the gas constant, and T is temperature. The quantity $\bar{\tau}$ is recalculated for each increment of the model deformation. Equations (A5) and (A6) express the fact that the viscous mode of deformation of crustal rocks is controlled by nonlinear, temperature-dependent dislocation flow [*Kirby,* 1983].

Kirby and Kronenberg [1986] expressed the nonlinear viscosity by

$$\dot{\gamma} = A\left(\sigma_1 - \sigma_3\right)^n e^{\frac{-Q}{RT}}$$

In this equation the rock parameters n and Q are the same as in (A5) and (A6). The relations between A and A_s were determined for $n = 2.4$ for three cases. If $\tau_{xy} \gg \tau_{xz}$, then $A \approx 0.6A_s$; if $\tau_{xy} = \tau_{xz}$, then $A \approx A_s$; and if $\tau_{xy} = \tau_{xz}/3$, then $A \approx 2.2A_s$. Our solutions are not sensitive to a factor of 2 change in the A coefficient (see the section on results). We thus assume that $A \approx A_s$.

Temperature is assumed to vary with depth according to equation (4–31) of *Turcotte and Schubert* [1982],

$$T = T_s + q_m \frac{z}{k} + (q_s - q_m) \frac{h_r}{k} \left\{ 1 - \exp\left(\frac{-z}{h_r} \right) \right\} \quad \text{(A7)}$$

where T_s is surface temperature, q_s is surface heat flux, q_m is the mantle heat flux, h_r is the characteristic length scale for the decrease of crustal radiogenic element concentration with depth, k is thermal conductivity, and z is depth. The temperature profile is assumed constant in time with no dependence on fault movement. In our model, the viscous constants A_s, n, and Q, and the elastic constants G and ν are assumed to be the same for the entire crust. Thus depth variations in rheology reflect only the variations of temperature with depth.

We used eight-node linear isoparametric finite elements (or bricks) to represent the spatial variation of the displacement and stress fields. With the linear isoparametric element, displacements vary linearly along the edges of each element. This element has one integration point, and the stress and strain have a single value within the element. The stress and strain values at the nodes are determined by averaging from the integration points in the neighboring elements (maximum of four elements in the present model). Standard Galerkin procedures, using linear isoparametric shape functions as weighting factors, are used to develop the discretized equations analogous to (A1)–(A6). The resulting system of linear algebraic equations is then solved after incorporating the equations representing the applied displacement boundary conditions. ABAQUS uses Newton's method because this method converges faster than alternate methods (modified Newton or quasi-Newton methods) [e.g., *Kikuchi*, 1986].

The antiplane strain condition (Figure 3) is enforced by setting the v, w displacement components at all nodes of the slice to zero, while the requirement that $\partial u/\partial x = 0$ is enforced by constraining the fault-parallel displacements at corresponding front and back surface nodes to be identical in the ABAQUS calculation.

The ABAQUS solutions are derived in increments. First, a displacement increment is applied to the boundaries of the model. This displacement increment is associated with a selected time increment and is thus equivalent to a velocity. Second, the program calculates the elastic strain (linear) associated with the displacement increment and the associated stresses. These stresses are substituted into (A5) to determine the incremental viscosity and the associated viscous strain rates. This procedure is iterated until equilibrium (A4) is achieved within the selected accuracy parameter. In ABAQUS, equilibrium is measured by ensuring that the out-of-equilibrium forces are smaller than the specified force tolerance. In the present computations the force tolerance is 5×10^9N; this value is small with respect to the average force at the nodes which is $3\text{–}4 \times 10^{12}$N.

ABAQUS provides a choice of an automatic time increment or a user-specified, constant time increment; we used the automatic time increment option. The computation starts with a user-defined initial time step of 0.1 year. ABAQUS monitors the stability of each step internally, and if the solution exceeds the selected tolerance, the program automatically switches to implicit time integration (backward difference) which is unconditionally stable. The size of the time increment during automatic time stepping is controlled by a user-supplied accuracy parameter which is 10^{-5} in the present computations. This value is the maximum permitted difference between the creep strain at the beginning of a computation increment and the creep strain at the end of that increment. If this value is exceeded anywhere in the mesh, the time increment is reduced automatically. The actual maximum differences in creep strain range from 10^{-6} to 10^{-14} during various steps of the computations. The higher value of 10^{-6} indicates that the maximum error of the stress is 0.025 MPa. The corresponding maximum error of the displacement is 0.01 mm; and the velocity error is negligible accordingly.

In a typical calculation over a 160-year earthquake cycle that uses the nonlinear viscous rheology of quartzite, the number of increments is 20 with 2–3 iterations in each increment. The shortest step is the initial user-defined step of 0.1 year, and the longest automatic step was ≈25 years. The number of equations solved in such model is ≈800, and the total solution time was ≈380 s of Cray YMP cpu time.

Appendix B: Comparison With the Model of Li and Rice [1987]

We have validated the application of the ABAQUS finite element code to problems involving earthquake related deformation by comparing numerical and analytic [*Li and Rice*, 1987] results for a simple model of the great earthquake cycle along the San Andreas fault. The model is illustrated in Figure B1. An elastic layer of thickness H overlies a viscoelastic layer of thickness h. Both layers are infinite in the horizontal x, y directions. A vertical fault along the x–z plane extends from the surface to a depth L within the elastic layer ($L \leq H$). The elastic and viscoelastic layers have shear moduli G and G_1, respectively; Poisson's ratio ν is the same in both layers. Far from the fault in the $\pm y$ directions there are imposed fault-parallel velocities $\pm v_p/2$. The fault is locked over its entire extent during the earthquake cycle time t_{cy}; after time t_{cy} has elapsed the fault is displaced suddenly to catch up to the accumulated displacements far from the fault. The cycle repeats indefinitely.

We have solved for the displacements and stresses in the elastic and viscoelastic layers exactly (to within numerical accuracy) with the finite element code ABAQUS. Numerical accuracy is mainly affected by both the fineness of the computational mesh and its overall size. The mesh is illustrated in Figure B1. Because of the symmetry about the fault plane it suffices to consider only $y > 0$. There is only one row of elements along the fault-parallel direction, a simplification made possible by the antiplane strain nature of the problem.

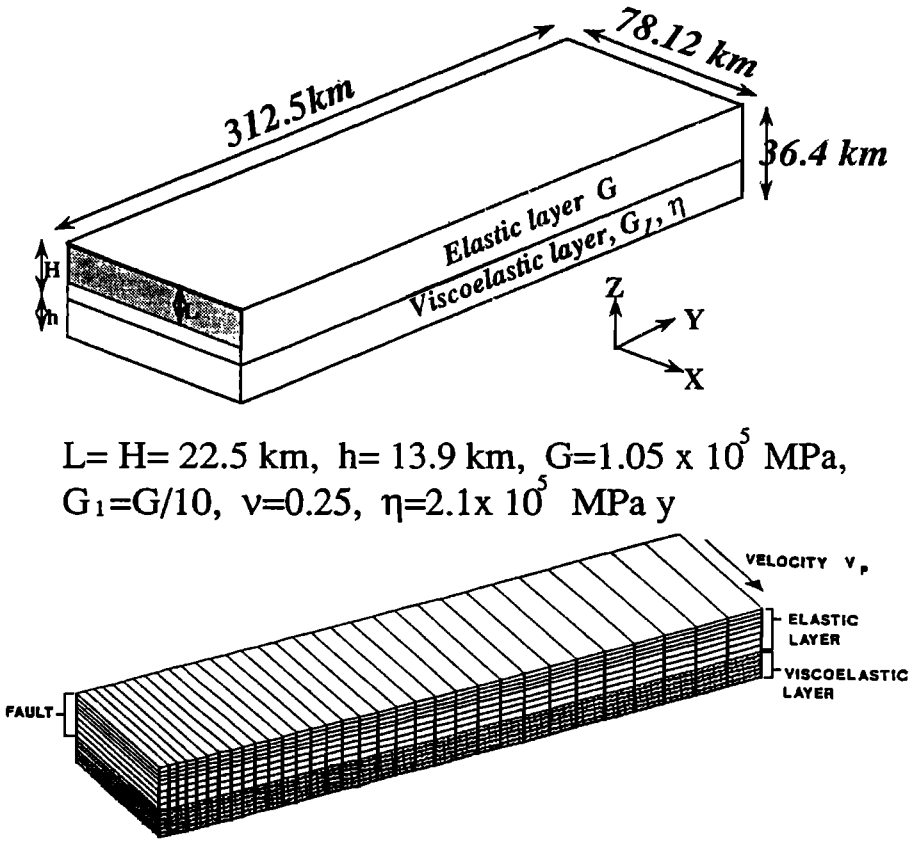

Figure B1. The model used to benchmark the ABAQUS solution versus the *Li and Rice* [1987] solution for great earthquakes along the San Andreas fault. (top) Model configuration following the *Li and Rice* setting; (bottom) computational mesh used in the ABAQUS numerical solution of the model at the top.

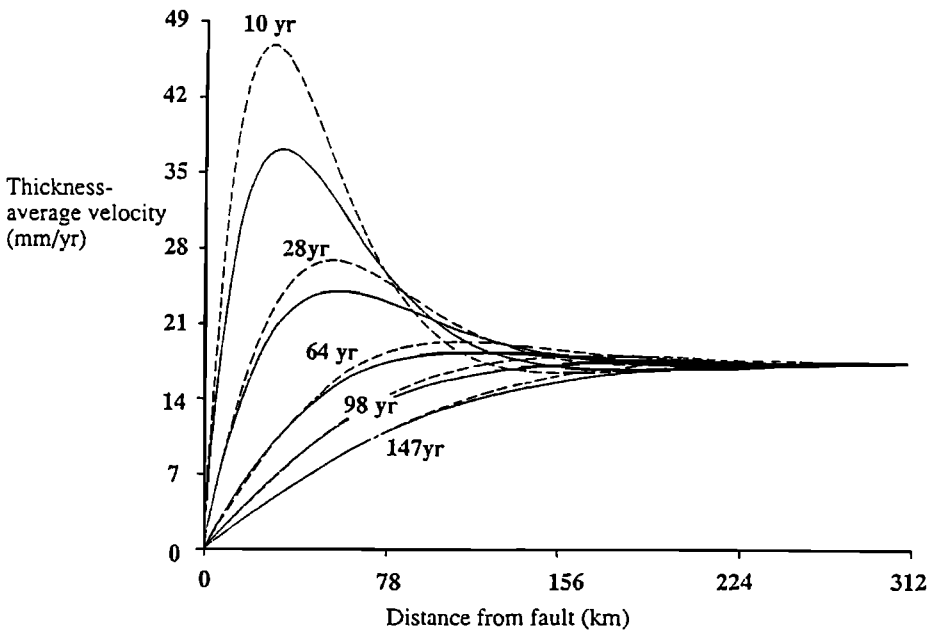

Figure B2. Thickness-averaged fault-parallel velocity of the elastic layer (normalized by v_p) versus distance perpendicular to the fault (normalized by H) at different times during the earthquake cycle. Results are shown for the ABAQUS finite element model and the generalized Elsasser model of *Li and Rice* [1987]. Parameters for the numerical finite element model include $G_1/G = 0.1$. For the generalized Elsasser model $b = 139$ km. Other parameter values are given in Appendix B.

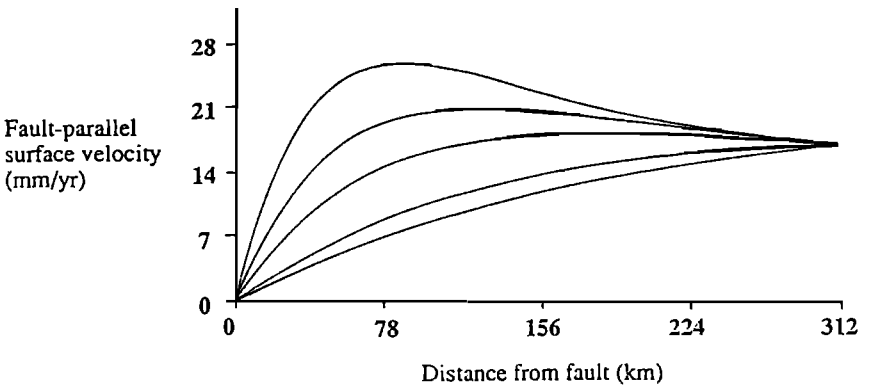

Figure B3. Fault-parallel surface velocity as a function of distance normal to the fault at different times during the earthquake cycle. Results are from the numerical finite element model. Parameter values and normalization are the same as in Figure B3.

The thicknesses of the elastic and viscoelastic layers are $H = 22.5$ km and $h = 13.9$ km. The mesh extends 312.5 km in the y direction perpendicular to the fault and contains 990 nodes and 448 elements. We consider the case of a through-going fault, i.e., $L = H$. Other parameter values are $t_{cy} = 160$ years, $G = 105$ GPa, $G_1 = 10.5$ GPa, $\nu = 0.25$, viscosity $\eta = 210$ GPa years (see Figure B1), and $v_p/2 = 17.5$ mm yr^{-1}. The choice of G and G_1 is discussed further below.

The boundary conditions for the numerical calculation are as follows. The end of the model far from and parallel to the fault is moved at the constant horizontal fault-parallel velocity $v_p/2$ for a time t_{cy}. The vertical velocity and the fault perpendicular velocity are zero on this end. The top surface is stress free. The bottom surface and the extension of the fault plane downward into the viscoelastic layer are also moved with the fault-parallel velocity $v_p/2$. The fault plane in the elastic layer is held fixed during t_{cy} and is displaced parallel to itself and horizontally by an amount $t_{cy}v_p/2$ during a very short time interval at the end of a cycle to catch up with the far end. The numerical model is exercised over a number of cycles to produce a quasi-steady solution. Before discussing the results of the numerical calculation, we briefly describe the analytic solution of *Li and Rice* [1987] with which we compare.

Li and Rice [1987] presented an analytic, albeit approximate solution to the problem described above. Their approach, based on a generalization of the Elsasser model [*Elsasser*, 1969; *Rice*, 1980; *Lehner et al.*, 1981], determines approximate layer-average displacements and stresses in the elastic layer. The viscoelastic layer is not treated explicitly; its affect on the elastic layer is approximately accounted for by a coupling pa-

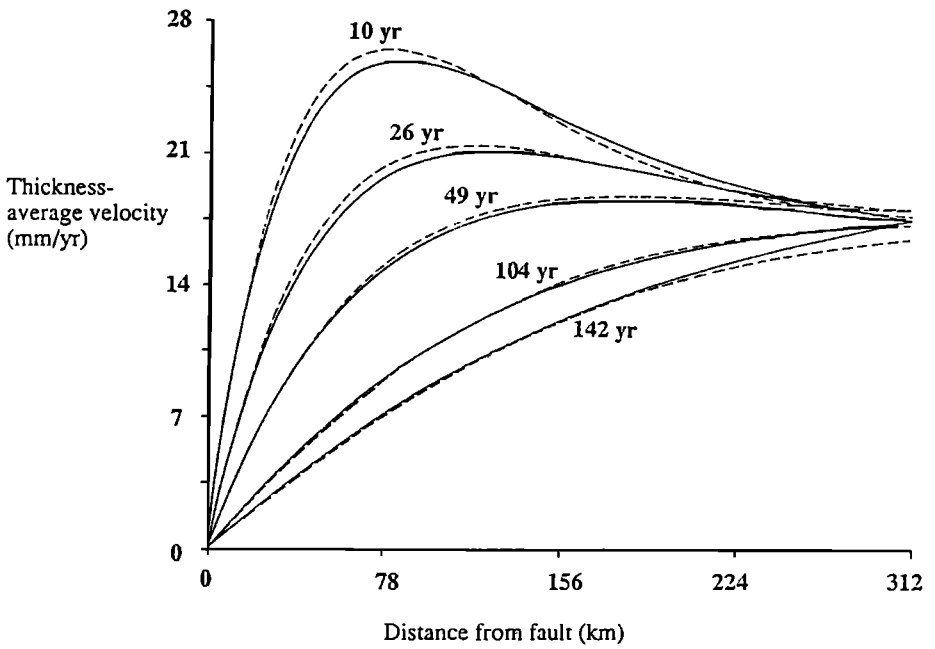

Figure B4. Similar to Figure B3 but for $G = G_1 = 35$ GPa and $b = 13.9$ km. In this case the generalized Elsasser solution does not provide a good match to the exact numerical solution at early times in the earthquake cycle when elastic behavior dominates the solution.

rameter b. The value of b is not uniquely determined but depends on the thicknesses of the layers and their rheological properties. The generalized Elsasser equation for the thickness-averaged fault-parallel displacement u in the elastic layer is [*Li and Rice*, 1987]

$$\frac{\partial u}{\partial t} = \left(\frac{HGh}{\eta} + bH\frac{\partial}{\partial t}\right)\frac{\partial^2 u}{\partial y^2} \qquad \text{(B1)}$$

It is the solution of the approximate equation (B1) with which we compare the exact numerical solution. The solution of (B1) depends on b, and there is no way to determine b for arbitrary values of H, h, G, G_1, and η. If $G_1 \ll G$, then b is approximated by hG/G_1 [*Lehner et al.*, 1981]. For this reason we took $G_1/G = 0.1$ as noted above. The corresponding value of b is then 139 km and the associated relaxation time $t_r = b\eta/Gh$ is 20 years.

Figure B2 shows the thickness-averaged fault-parallel velocity in the elastic layer (normalized by v_p) at different times during the earthquake cycle versus perpendicular distance from the fault (normalized by the elastic layer thickness) for the *Li and Rice* [1987] model and our numerical model. The numerical model was run for five cycles and the results are plotted for corresponding times in the fifth cycle, i.e., 648.7 years= 4 × 160 years +8.7 years. Agreement between the numerical and approximate analytic models is excellent at all times during the earthquake cycle. The small disagreement at large distances from the fault late in the cycle (Figure B2, time = 142.5 years) is a consequence of the numerical model not being quite long enough; i.e., the numerical model should have extended somewhat farther from the fault.

The behavior of ground deformation during the earthquake cycle is illustrated in Figure B3 by the plot of normalized fault-parallel surface velocity versus normalized distance from the fault for different times during the cycle (based on the numerical results). The peak in velocity at early times is due to the sudden displacement of the fault at the end of the previous earthquake cycle. The peak decays with time and moves outward from the fault with time due to the viscous traction at the base of the elastic layer.

The limitations of the generalized Elsasser model are illustrated by the results shown in Figure B4. In this case only the values of G and G_1 have been changed to $G = G_1 = 35$ GPa and all other parameters are as before. Since G_1 is not small compared with G, another way of determining b is required. *Li and Rice* [1987] suggest the use of $b = \pi^2 H/16$, a value appropriate to a mode III crack in an infinite elastic half-space of uniform shear modulus G. While G is uniform in the case of Figure B4, deformation occurs in superposed elastic and viscoelastic layers of finite thickness, not in an elastic half-space. The approximate analytic solution in Figure B4 was computed with $b = \pi^2(22.5 \text{ km})/16 = 13.9$ km and $t_r = 6$ years. The numerical results shown in Figure B4 are from the last cycle of a four-cycle calculation.

The approximate analytically determined values of thickness-averaged fault-parallel velocity in the elastic layer as a function of distance from the fault (Figure B4) agrees closely with the exact numerical solution at times late in the earthquake cycle when viscous relaxation effects are important. However, the approximate analytic result is not a good representation of the exact solution early in the earthquake cycle when the elastic response of the coupled layers dominates. The inability of the analytic solution to match the exact solution is probably a consequence of the choice of the b value. There is no general prescription for determining b; indeed, the "correct" value of b can only be obtained a posteriori by fitting the exact numerical solution. This is a basic limitation of the generalized Elsasser model.

In summary, we have benchmarked the numerical finite element code against the approximate analytic solution of *Li and Rice* [1987] with a choice of model parameter values for which the analytic solution is close to being exact. We then used the exact numerical solution, with another choice of model parameters, to demonstrate the approximate nature and limitations of the analytic solution.

Acknowledgments. The authors are grateful to Nannette Anderson for her help in the preparation of this paper. The thorough reviews of Roger Denlinger, Stephen Hickman,and James Savage contributed to significant improvement of the manuscript. The work was supported by grants from the Institute of Geophysics and Planetary Physics at the Los Alamos National Laboratory, the NASA Geodynamics program (NAGW 2646),and the U.S.-Israel Bi-national Science Fund grant (86-183). The ABAQUS code was developed by HKS Inc., Pawtucket, Rhode Island.

References

Brace, W. F., and D.L. Kohlstedt, Limits on lithospheric stress imposed by laboratory experiments, *J. Geophys. Res., 85*, 6248–6252, 1980.

Elsasser, W. M., Convection and stress propagation in the upper mantle, in *The Application of Modern Physics to the Earth and Planetary Interiors*, edited by S. K. Runcorn, pp. 223–246, Wiley-Interscience, New York, 1969.

Fuis, G. S., and W. D. Mooney, Lithospheric structure and tectonics from seismic-refraction and other data, in *The San Andreas Fault System, California*, edited by R. E. Wallace, *U.S. Geol. Surv. Prof. Pap., 1515*, 207–238, 1990.

Kikuchi, N., *Finite Element Methods in Mechanics*, 418 pp., Cambridge University Press, New York, 1986.

Kirby, S. H., Rheology of the lithosphere, *Rev. Geophys., 21*, 1458–1487, 1983.

Kirby, S. H., and A. K. Kronenberg, Rheology of the lithosphere: Selected topics, *Rev. Geophys., 25*, 1219–1244, 1986.

Lachenbruch, A. H., and J. H. Sass, Heat flow and energetics of the San Andreas fault zone, *J. Geophys. Res., 85*, 6185–6222, 1980.

Lehner, F. K., V. C. Li, and J. R. Rice, Stress diffusion along rupturing plate boundaries, *J. Geophys. Res., 86*, 6155–6169, 1981.

Li, V. C., and J. R. Rice, Crustal deformation in great California earthquake cycles, *J. Geophys. Res., 92*, 11,533–11,551, 1987.

Lisowski, M., J. C. Savage, and W. H. Prescott, The velocity field along the San Andreas fault in central and southern California, *J. Geophys. Res., 96*, 8369–8389, 1991.

Lyzenga, G. A., A. Raefsky, and S. G. Mulligan, Models of recurrent strike-slip earthquake cycles and the state of crustal stress, *J. Geophys. Res., 96*, 21,623–21,640, 1991.

Nur, A., and G. Mavko, Postseismic viscoelastic rebound, *Science, 183*, 204–206, 1974.

Oppenheimer, D. H., and J. P. Eaton, Moho orientation beneath central California from regional earthquake travel times, *J. Geophys. Res., 89*, 10,267–10,282, 1984.

Oppenheimer, D. H., P. A. Reasenberg, and R.W. Simpson, Fault plane solutions for the Morgan Hill, California, earthquake sequence: Evidence for the state of stress on the Calaveras fault, *J. Geophys. Res., 93*, 9007–9026, 1988.

Prescott, W. H., and S.-B. Yu, Geodetic measurements of horizontal deformation in the northern San Francisco Bay region, California, *J. Geophys. Res., 91*, 7475–7484, 1986.

Reid, H. F., The California earthquake of April 18, 1906: The mechanics of the earthquake, vol.2, *Publ. Carnegie Inst. Washington, 87*, 192 pp., 1910.

Rice, J. R., The mechanics of earthquake rupture, in *Physics of the Earth's Interior*, edited by A. M. Dziewonski and E. Boschi, pp. 555–649, North-Holland, New York, 1980.

Savage, J. C., and W. H., Prescott, Asthenospheric readjustment and the earthquake cycle, *J. Geophys. Res., 83*, 3369–3376, 1978.

Sieh, K., M. Stuiver, and D. Brillinger, A more precise chronology of earthquakes produced by the San Andreas fault in southern California, *J. Geophys. Res., 94*, 603–623, 1989.

Thatcher, W., Strain accumulation and release mechanism of the 1906 San Francisco earthquake, *J. Geophys. Res., 80*, 4862–4872, 1975.

Thatcher, W., Nonlinear strain buildup and the earthquake cycle on the San Andreas fault, *J. Geophys. Res., 88*, 5893–5902, 1983.

Turcotte D. L., and G. Schubert, *Geodynamics*, 450 pp., John Wiley, New York, 1982.

Turcotte, D. L., J. Y. Liu and F. H. Kulhawy, The role of intracrustal asthenosphere on the behavior of major strike-slip faults, *J. Geophys. Res., 89*, 5801–5816, 1984.

Ward, S. N., Pacific-North America plate motions: New results from very long baseline interferometry, *J. Geophys. Res., 95*, 21,965–21,981, 1990.

C. Anderson, Group ESE–13, MS J576, Los Alamos National Laboratory, (e-mail: canderson@esa.lanl.gov)

Z. Reches, Department of Geology, Institute of Earth Sciences, The Hebrew University of Jerusalem, Givat-Ram, Jerusalem 91904, Israel (e-mail: reches@vms.huji.ac.il)

G. Schubert, Department of Earth and Space Sciences, and Institute of Geophysics and Planetary Physics, University of California, Los Angeles, CA 90024–1567 (e-mail: gschubert@mgnvax.ess.ucla.edu)

(Received September 8, 1992; revised January 24, 1994; accepted January 31, 1994.)